RSC Advances

PAPER

View Article Online
View Journal | View Issue

Cite this: *RSC Adv.*, 2025, **15**, 36393

Controlled formation of closed-pore structures in modified phenolic resin-derived carbons for enhanced sodium storage

Liwei Wang,[ab] Yuming Hu,[ab] Yuhao Wang,[ac] Xue Nie,[ab] Zixuan Lei,[a] Congyan Hu,[ab] Li Ye,[a] Yiming Yang,*[a] Tong Zhao*[ab] and Hao Li*[ab]

Hard carbon anodes face the critical challenge of low initial coulombic efficiency (ICE) and capacity fading arising from insufficient control of the closed-pore structure, which must be addressed to advance sodium-ion batteries (SIBs). In this work, we present a carbon structure engineering strategy to enhance anode performance by treating cyano-functionalized phenolic resin-derived carbon microspheres with NH_3. Cyano side groups increase crosslinking density during resin curing, facilitating the formation of closed-pore structures with low specific surface areas. Stepwise carbonization in ammonia and nitrogen atmospheres tailors the closed-pore structure and surface morphology. Small-angle X-ray scattering (SAXS) and high-resolution transmission electron microscopy (HR-TEM) reveal that the closed-pore walls undergo mild etching, inducing pore surface defects. Compared with nitrogen treatment, NH_3 significantly enhances nitrogen incorporation and electrochemical activity. The optimized sample carbonized at 1200 °C exhibits a specific surface area of 1.87 $m^2\ g^{-1}$, an ICE of 81.81%, and a first-cycle discharge capacity of 373.3 mAh g^{-1} at a current density of 30 mA g^{-1}. *In situ* X-ray Diffraction (XRD) and the galvanostatic intermittent titration technique (GITT) reveal a three-step sodium storage mechanism: adsorption, intercalation, and pore-filling, with rough pore surfaces accelerating filling kinetics. This strategy provides a scalable approach for designing high-performance carbon-based anodes.

Received 18th July 2025
Accepted 19th September 2025

DOI: 10.1039/d5ra05188f

rsc.li/rsc-advances

1 Introduction

As the search for more sustainable and scalable battery technologies intensifies, sodium-ion batteries (SIBs) have emerged as a compelling alternative to conventional lithium-based systems.[1] However, the development of high-performance and low-cost anode materials remains a key challenge in advancing SIB technology.[2] Graphite is well established as a commercial anode in lithium-ion batteries, though its narrow interlayer spacing restricts sodium-ion storage.[3] Metal oxide anodes can provide high capacities, but their use is hindered by large volume changes and poor cycling stability.[4] In comparison, hard carbon combines favorable electrical properties, low cost, and resource abundance, and is widely recognized as a promising anode material.[5]

Hard carbon provides effective pathways for sodium-ion insertion and extraction through its disordered graphene layers, large interlayer spacing (>0.37 nm), structural defects, and vacancies.[6] Hard carbon is typically synthesized by carbonizing thermosetting polymers (such as phenolic resins) or non-graphitizable organic precursors (such as biomass residues, cellulose, and sucrose) at temperatures above 1000 °C.[2,7,8] During high-temperature pyrolysis, organic functional groups decompose and the carbon atoms gradually rearrange into a disordered lamellar structure with enlarged interlayer spacing, leading to the formation of hard carbon. Recent research has focused on several strategies to improve the electrochemical performance of hard carbon anodes. First, incorporating heteroatoms such as nitrogen, oxygen, phosphorus, and sulfur into the carbon framework has been widely explored. This approach increases defect density, creates more sodium-ion adsorption sites, and modulates the electronic structure, contributing to improved storage capability.[9] Second, tailoring the pore structure, especially achieving a balanced distribution of open and closed pores, plays a crucial role in facilitating ion transport and improving capacity retention. Among these approaches, the control of closed-pore structures has received increasing attention, particularly for improving the low-voltage capacity below 0.1 V (*vs.* Na^+/Na). Closed pores are recognized as essential sodium-ion storage sites, and their quantity, size, and surface properties directly impact the plateau capacity and overall energy density of sodium-ion batteries.[10–12]

[a]*Key Laboratory of Science and Technology on High-tech Polymer Materials, Institute of Chemistry Chinese Academy of Sciences, Beijing, 100190, China. E-mail: yiming924@iccas.ac.cn; tzhao@iccas.ac.cn; lihao306@iccas.ac.cn*

[b]*University of Chinese Academy of Sciences, Beijing, 100049, China*

[c]*CAS Key Laboratory of Molecular Nanostructure and Nanotechnology, Institute of Chemistry Chinese Academy of Sciences, Beijing, 100190, China*

In recent years, considerable research has focused on the impact of carbon material regulation on pore structure. For example, Sun *et al.* found that the carbon chain length in the precursor could effectively control the rearrangement behavior of carbon layers during high-temperature carbonization, leading to the formation of various pore structures ranging from closed pores to open pores, thereby significantly influencing the electrochemical performance.[13] Hu *et al.* reported the effect of carbonyl groups towards closed-pore structure during pyrolysis process.[14] The hard carbon with optimized closed pore structure demonstrated excellent cycling stability, delivering a reversible capacity of 360.96 mAh g^{-1} at 30 mA g^{-1} and retaining 94% of its capacity after 500 cycles at 1 A g^{-1}. Yang *et al.* achieved independent control of pore size distribution by treating carbonized walnut shell with hexadecyl trimethyl ammonium bromide under hydrothermal conditions.[15] The resulting hard carbon material, rich in mesopores, exhibited an outstanding cycling capacity of 283.7 mAh g^{-1} at a current density of 20 mA g^{-1}.

Combining heteroatom doping with pore structure regulation can further refine the structure of hard carbon, and is widely regarded as an effective strategy to improve its sodium storage performance. Tao *et al.* developed a mesoporous hard carbon derived from soybean roots through N, P co-doping (NPDC), which enlarged the interlayer spacing and increased the number of active sites.[16] The optimized NPDC exhibited excellent cycling stability, delivering a capacity of 197 mA g^{-1} after 2000 cycles at a current density of 2.0 A g^{-1} in sodium-ion batteries. Liu *et al.* found that high-temperature sintering led to a 3.9 mol% increase in nitrogen content compared to the high-pressure hydrothermal process.[17] At the same time, the micropore ratio reached as high as 93.6%, indicating that the structure was predominantly composed of closed micropores. Pyrrolic nitrogen and other nitrogen-containing functional groups introduced during this process provided abundant Na^+ adsorption sites, thereby enhancing the battery capacity. As a result, the fabricated HP-NHC electrode delivered a high reversible capacity of 331 mAh g^{-1} after 200 cycles at a current density of 0.5 A g^{-1}. Zhong *et al.* prepared novel nitrogen-doped carbon spheres with mesopores, ultrathin nanostructures, and optimized graphitization through a three-step process.[18] Benefiting from the unique mesoporous architecture and well-regulated nitrogen content, the number of sodium-ion adsorption sites was significantly increased. As a result, the sample exhibited excellent sodium storage performance, delivering a high reversible capacity of 334.7 mAh g^{-1} at 50 mA g^{-1} and maintaining an outstanding rate capability of 93.9 mAh g^{-1} even at 5 A g^{-1}. Such studies on leveraging the synergistic effect of carbon layers to enhance cycling stability and electrochemical performance demonstrate that structural and compositional co-optimization is broadly applicable across different systems.[19]

Although both pore structure regulation and heteroatom doping have been widely employed for the targeted engineering of carbon materials, most studies have mainly focused on the effects of pore size and distribution on the performance of sodium-ion batteries, with little attention paid to the role of pore surface characteristics. Enhancing the surface roughness of closed pores while maintain low specific surface area for hard carbon holds great potential for achieving a favorable balance between high ICE and excellent sodium storage capacity.[20,21]

In this work, we present a carbon structure engineering strategy to enhance the sodium storage performance of hard carbon by treating cyano-functionalized phenolic resin-derived carbons with NH_3. Through the introduction of cyano side groups, the crosslinking density of the precursor resin is significantly increased, promoting the formation of hard carbon micropheres with low specific surface area (SSA), as well as closed-pore structures with smooth surface. During carbonization in an NH_3 atmosphere, the pore walls undergo mild etching, leading to the generation of surface defects, while simultaneously enabling the incorporation of active nitrogen species into the carbon matrix. This dual-nitrogen-source doping strategy effectively optimizes the closed pore microstructure and chemical composition of the carbon material without compromise of low SSA, leading to enhanced sodium-ion diffusion kinetics, increased reversible capacity, and improved cycling stability. The hard carbon structure prepared *via* this strategy exhibits an ultra-low specific surface area of 1.87 m^2 g^{-1}. Based on this, the assembled sodium-ion half-cell delivers a first-cycle discharge capacity of 373.3 mAh g^{-1} with an initial coulombic efficiency of 81.81%. Moreover, it retains 97.2% of its capacity after 200 cycles. This work provides a feasible and scalable approach for the design of high-performance carbon-based anodes, offering valuable insights into the future development of advanced sodium-ion batteries.

2 Materials and methods

2.1 Materials

2.1.1 Synthesis of PN microspheres. PMMA (20 g) was dissolved in 300 mL of acetone in a three-necked flask under reflux at 75 °C in a water bath. After complete dissolution, 60 g of cyano-modified phenolic resin (PN) was added and stirred thoroughly to form a homogeneous solution. The acetone was then evaporated until the mixture became viscous, followed by thermal curing in an oven through a stepwise heating process: first to 170 °C for 1 h, then to 200 °C for another 1 h, and finally to 280 °C for 4 h. The cured product was carbonized in a tubular furnace under different conditions. For the N_2-carbonized samples, the cured resin was heated to 500 °C with a heating rate of 5 °C min^{-1} and kept for 1 h under nitrogen, followed by heating to 800 °C for 2 h, and then to the final temperatures of 1000 °C, 1200 °C, 1400 °C, or 1600 °C, each held for 2 h. The resulting products were denoted as PNHC-T1000, PNHC-T1200, PNHC-T1400, and PNHC-T1600, respectively. For the NH_3-modified samples, the cured resin was firstly heated to 500 °C under NH_3 for 1 h, followed by switching to nitrogen atmosphere and continuing the same heating process as above. The final products were denoted as NPNHC-T1000, NPNHC-T1200, NPNHC-T1400, and NPNHC-T1600, respectively.

2.1.2 Physical characterizations. The surface morphology of the materials was observed using a scanning electron microscope (SEM, Hitachi SU-8020), and the microstructure was

analyzed by high-resolution transmission electron microscopy (HRTEM, JEOL JEM-F200) combined with selected area electron diffraction (SAED). The crystal structure of the materials was characterized by X-ray diffraction (XRD, Rigaku SmartLab) at a scan rate of 6° per min. Raman spectra were obtained using a LabRAM HR Evolution spectrometer with a 532 nm laser wavelength. The elemental composition of the materials was determined using an elemental analyzer (Thermo Flash Smart), and the chemical states of the elements were analyzed by X-ray photoelectron spectroscopy (XPS, Thermo Fisher Scientific, ESCALAB 250XI). The specific surface area and pore size distribution were measured using a surface area analyzer (Micromeritics ASAP 3030) and calculated by the Brunauer–Emmett–Teller (BET) method. The closed-pore structure was investigated by small-angle X-ray scattering (Xeuss 2.0).

2.1.3 Electrochemical measurements. CR2032-type coin cells were assembled in an argon-filled glove box with both oxygen and moisture levels below 5 ppm. The working electrodes were prepared by mixing the active materials (89 wt%), Super P conductive carbon (5 wt%), and polyvinylidene fluoride (PVDF) binder (6 wt%) in *N*-methyl-2-pyrrolidone (NMP) to form a homogeneous slurry. The slurry was coated on aluminum foil and dried at 110 °C for 2 h in a convection oven. The electrodes were then punched into 12 mm discs, weighed, and further dried in a vacuum oven at 65 °C overnight. The mass loading of active materials was approximately 3.8 mg cm^{-2}. Sodium metal foil was used as the counter/reference electrode. The electrolyte was composed of 1 M $NaPF_6$ dissolved in a mixture of ethylene carbonate (EC) and dimethyl carbonate (DMC) in a 1 : 1 volume ratio, with an electrolyte volume of 200 μL per cell. Glass fiber membranes were used as the separators. Galvanostatic charge/discharge tests were carried out using a battery testing system (LAND CT2001A) within a voltage window of 0–2.5 V at various current densities. Cyclic voltammetry (CV) measurements were conducted on CHI660E electrochemical workstation at a scan rate of 0.5 mV s^{-1} in the same voltage range. Electrochemical impedance spectroscopy (EIS) was performed at open circuit voltage with an AC amplitude of 5 mV over a frequency range from 10^5 to 10^{-2} Hz. The mobility of sodium ions within the carbon electrode was investigated using galvanostatic intermittent titration technique (GITT). In this method, short current pulses are applied to the cell, and the voltage response is recorded both during the pulse and during the subsequent relaxation period when no current is applied. For *in situ* electrochemical XRD measurements, the *in situ* battery was placed horizontally on the sample stage with the beryllium window facing upward, ensuring that the X-ray beam was aligned with the center of the beryllium window. The battery was connected to the electrochemical testing system and left at rest for 6 hours. Then, a full charge–discharge cycle was carried out at a current rate of 0.1C (based on a nominal specific capacity of 300 mAh g^{-1}) within a voltage range of 0–2.5 V. Simultaneously, the XRD scanning program was initiated with a scanning range of 10–40° and a scan rate of 3° per min. The XRD measurements were conducted continuously in a loop until the completion of the charge–discharge cycle. All electrochemical tests were conducted at room temperature.

3 Results and discussion

In this work, carbon precursor microspheres were successfully constructed *via* reaction-induced phase separation by curing reaction of PN/PMMA blend. As illustrated in Fig. 1(a), PN and PMMA initially formed a homogeneous solution in acetone, followed by solvent evaporation to prepare viscous blend. During the subsequent heating and curing process, the blend displayed thermally induced phase separation accompanied by phase inversion behavior, where thermoplastic PMMA gradually transformed into the continuous phase, while thermoset PN resin crosslinked into the dispersed phase to form spherical domains. This process was governed by the combined effects of thermodynamic driving forces and kinetic factors, exhibiting typical characteristics of a binodal decomposition mechanism. To achieve precise morphological control, a stepwise thermal curing strategy was adopted to reduce the reactivity of PN resin, effectively suppressing premature and irregular crosslinking. As a result, well-regulated phase-separated structures were formed, yielding monodisperse PN microspheres with uniform particle size distribution. During the carbonization process, the thermally unstable PMMA decomposed into gaseous products, leaving behind only the carbonized microspheres derived from PN. In addition, the residual acetone trapped within the crosslinked network may introduce extra free volume within the resin network, which could further lead to the formation of closed-pore structures upon pyrolysis. As shown in Fig. 1(b_1–b_4) and (c_1–c_4), both PNHC and NPNHC samples exhibit uniform spherical morphology with smooth surface and narrow particle size distributions, PNHC showed average diameters of 1.58 ± 0.36 μm and 1.33 ± 0.23 μm for NPNHCs, statistical analysis indicated no significant difference whether the obtained carbon microsphere were NH_3 treated. High-resolution TEM images (Fig. 1(b_3) and (c_3)) reveal a typical disordered carbon structure composed of short-range turbostratic graphene layers, while the corresponding selected area electron diffraction (SAED) patterns (Fig. 1(b_4) and (c_4)) display diffuse rings, further confirming the amorphous nature and characteristic short-range ordering of hard carbon.[6,22]

The hard carbon structure of microspheres are further characterized and the results are showed in Fig. 2. The crystallographic structure of the carbon samples are characterized by X-ray diffraction (XRD), as shown in Fig. 2(a) and (e). All samples exhibit two broad diffraction peaks located at approximately 24° and 44°, corresponding to the (002) and (100) planes of carbon, indicating typical turbostratic carbon structures. As the carbonization temperature increases, the (002) peak becomes narrower and sharper and shifts toward higher angles, reflecting enhanced structural ordering and reduction in interlayer spacing (d_{002}).[6,22] Specifically, as shown in Fig. 2(c) and (g), for the PNHC-T series, the d_{002} value decreases from 0.381 nm at 1000 °C to 0.363 nm at 1600 °C, while the stacking height (L_c) increases from 0.66 nm to 0.92 nm, indicating a progressive improvement in degree of graphitization with the increasing temperature. As for NPNHC series, the d_{002} value decreases from 0.374 nm to 0.365 nm when temperature increases from

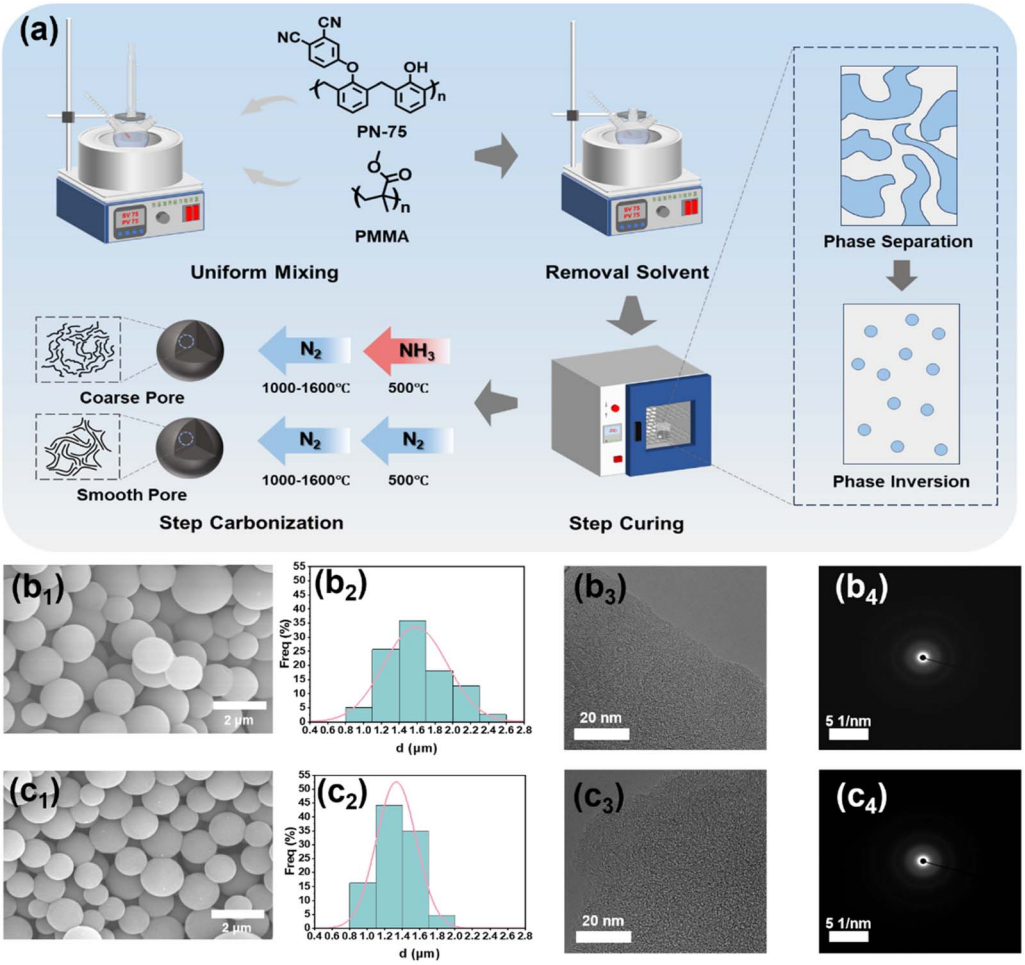

Fig. 1 (a) Schematic illustration of the synthesis and carbonization process of PNHC and NPNHC; (b_1) the morphology of PNHC-T1200 obtained from SEM image, (b_2) particle size distribution diagram, (b_3) the carbonized structure revealed by HRTEM image, and (b_4) SAED pattern; (c_1) the morphology of NPNHC-T1200 obtained from SEM image, (c_2) particle size distribution diagram, (c_3) the carbonized structure revealed by HRTEM image, and (c_4) SAED pattern.

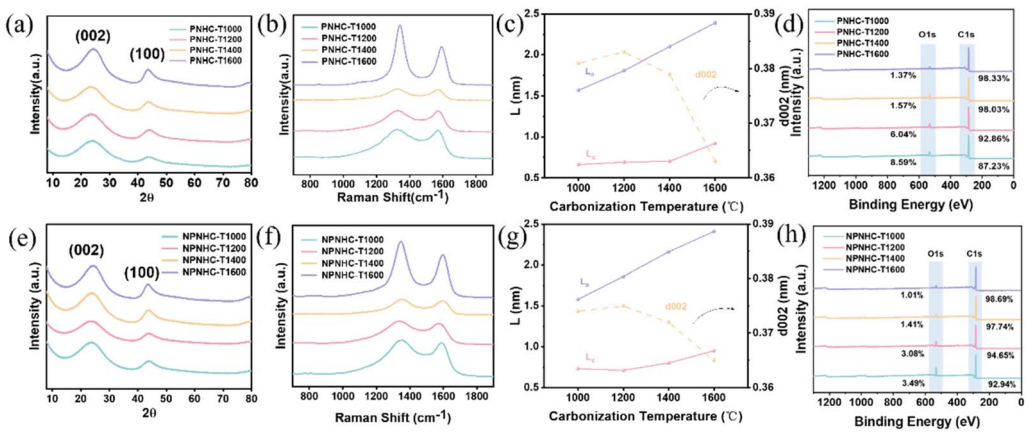

Fig. 2 Structural characterization of PNHC materials at different carbonization temperatures: (a) XRD patterns (the diffraction peaks located at around 22–25° and 43–45° can be indexed to the (002) and (100) planes of carbon (graphite, JCPDS No. 41-1487)), (b) Raman spectra, (c) relationship between carbonization temperature and crystallite stacking height L_c, in-plane crystallite size L_a, and interlayer spacing d_{002}, and (d) high-resolution XPS spectra. Structural characterization of NPNHC materials at different carbonization temperatures: (e) XRD patterns, (f) Raman spectra, (g) relationship between carbonization temperature and L_c, L_a, and d_{002}, and (h) high-resolution XPS spectra.

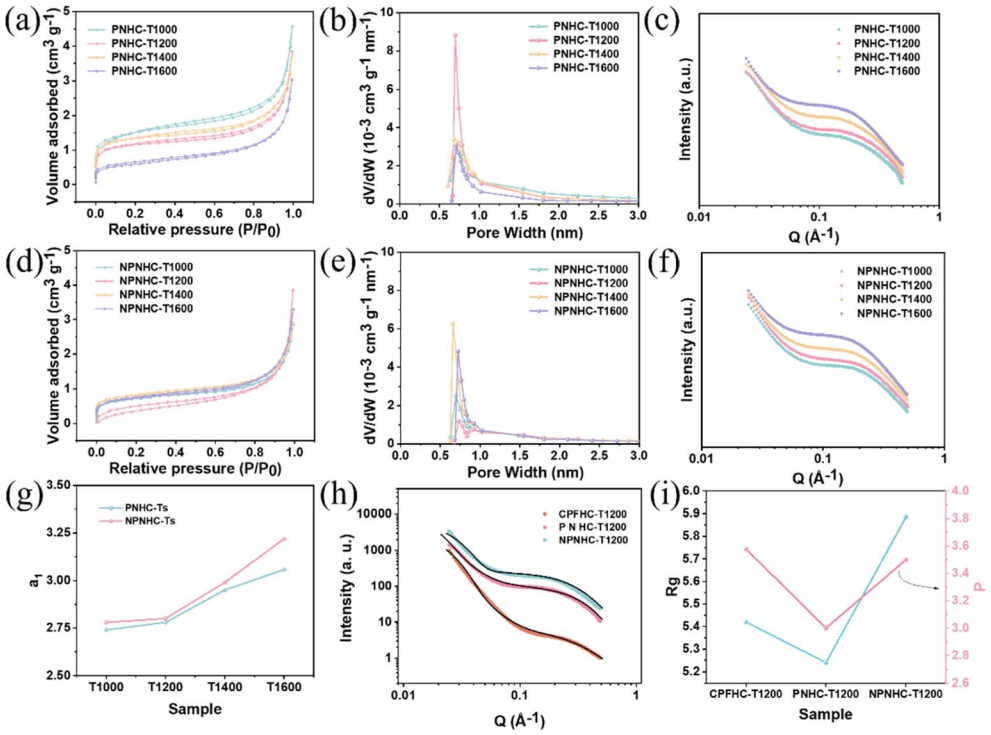

Fig. 3 (a–c) Nitrogen adsorption/desorption isotherms (a), pore size distributions (b), and small-angle X-ray scattering (SAXS) curves (c) of PNHC materials carbonized at different temperatures; (d–f) nitrogen adsorption/desorption isotherms (d), pore size distributions (e), and SAXS curves (f) of NPNHC materials carbonized at different temperatures; (g) characteristic length (a_1) obtained by Debye model fitting; (h) SAXS curves and corresponding Unified fitting results of three types of carbon spheres carbonized at 1200 °C; (i) radius of gyration (R_g) and surface roughness parameter (P) obtained by Unified fitting.

1000 °C to 1600 °C, while the stacking height (L_c) increases from 0.73 m to 0.95 m. Compare to PNHCs, NPNHCs exhibited higher degree of graphitization at lower temperature, but further ordering of graphite layer was prohibited at 1600 °C. This indicates that NH_3 treatment effectively promotes carbon layer stacking and enhances structural ordering at lower temperature, but also bring defects and nitrogen-doping in the graphite planes, which reduce the further graphitization as temperature increase.[10,23] Among them, the NPNHC-T1200 sample exhibits a moderate d_{002} value and L_c value, which is favorable for constructing a balanced conductive framework while maintaining sodium-ion intercalation pathways, potentially achieving a better trade-off between ICE and reversible capacity.

The Raman spectra of the two types of carbon spheres are shown in Fig. 2(b) and (f). Based on the Gaussian–Lorentz fitting results in Fig. S1 and S2, the I_D/I_G ratio gradually decreases with increasing carbonization temperature, indicating an enhanced graphitization degree in both PNHC and NPNHC samples. The calculated L_a values, presented in Fig. 2(c) and (g), clearly show a progressive increase with increasing temperature.[24,25] The Raman spectra results showed good agreement with the XRD results that overall an enhanced graphitization degree was achieved at higher temperature, PNHCs and NPNHCs remained their hard carbon nature until 1600 °C.

Elemental analysis was performed on the carbon microspheres, as shown in Fig. 2(d) and (h), and the results indicate that with increasing carbonization temperature, the carbon content gradually increases, while the nitrogen and oxygen contents decrease, indicating a further degree of carbonization. Compared with PNHCs, NPNHCs exhibit higher carbon content and lower oxygen content at 1000 °C and 1200 °C, which is favorable for enhancing electronic conductivity and structural stability. This may be attributed to the removal of oxygen containing functional group by NH_3 treatment at 500 °C, which enables NPNHCs to have better conductivity.[26] In addition, NPNHCs show higher nitrogen content at low temperatures, further confirming that NH_3 treatment enables effective nitrogen doping during the early stages of carbonization. It is noteworthy that regardless of the total nitrogen retention, nitrogen in the carbonized samples predominantly exists in the forms of pyridinic N, pyrrolic N, and graphitic N, which together improve electrochemical performance. Specifically, pyridinic and pyrrolic nitrogen help provide active sites for sodium storage, while graphitic nitrogen contributes to improved electronic conductivity.[16,27] Compared with PNHCs, NPNHCs retain a higher overall nitrogen content at the lower carbonization temperatures of 1000 °C and 1200 °C, resulting in more pronounced synergistic regulation by the nitrogen species and further enhancement of electrochemical performance.

The open pore structure and closed pore structure were further analyzed in Fig. 3. Nitrogen adsorption–desorption measurements were conducted to evaluate the surface pore structure of the carbon materials, and the corresponding isotherms are shown in Fig. 3(a) and (d). Both PNHC and

NPNHC samples exhibit typical type IV nitrogen adsorption isotherms, with significant adsorption in the low relative pressure region (P/P_0 < 0.1), indicating that both materials are predominantly microporous.[28,29] Meanwhile, the presence of a hysteresis loop at higher relative pressures and the pore size distribution curves in Fig. 3(b) and (e) suggest that mesopores are also present, thus endowing the materials with hierarchical micro-meso-macro pore structures, in line with recent reports.[30] The pore sizes of both series of samples are primarily concentrated in the range of 0.5–1 nm, characteristic of typical microporous structures. It should be noted that the appearance of some larger pores may also be associated with interparticle voids or partial separation of aggregates during sample handling, rather than being entirely intrinsic to the carbon spheres. Nevertheless, such features are often considered as part of the hierarchical micro-meso-macro pore structures.

Due to the inherently high crosslinking density of the PN75 resin, the resulting carbon materials generally exhibit low specific surface areas. Under identical carbonization conditions, the specific surface areas of the PNHC series are 5.39, 4.24, 4.95, and 2.32 $m^2\ g^{-1}$ at 1000 °C, 1200 °C, 1400 °C, and 1600 °C, respectively, while those of the NPNHC series are 2.66, 1.87, 2.99, and 2.77 $m^2\ g^{-1}$. Except at 1600 °C, the NPNHC samples consistently exhibit lower surface areas than their PNHC counterparts, indicating that the introduction of NH_3 not only preserves the dense structure afforded by the high crosslinking degree, but may also suppress further micropore development during carbonization. As a result, the NPNHC materials maintain good structural stability while retaining low specific surface areas, which is beneficial for improving the ICE. A low specific surface area helps reduce irreversible reactions with the electrolyte, thereby enhancing the ICE.[31] Meanwhile, the characteristics of the closed-pore structure determine whether sodium ions can access the internal regions of the material and participate in electrochemical reactions, thus contributing to the overall capacity. Therefore, despite limited differences in total surface area, the variation in closed-pore microstructure remains a key factor influencing sodium storage behavior and warrants further investigation.[32]

To further clarify the microstructural features developed during carbonization, SAXS measurements are performed and obtained curves are fitted by debye equation to investigate the presence of nanoscale close pore structures within the samples. As shown in the Fig. 3(c) and (f), all samples exhibit similar SAXS profiles, with scattering intensity gradually sharply decrease at low q region and pronounced shoulder appears in the range of 0.03–0.4 $Å^{-1}$, indicating the presence of a considerable number of nanometer-sized closed pores within the carbon matrix.[6] As temperature increases, the shoulder peaks show enhanced relative intensity and gradually shift to lower q, confirming the higher pore volume and larger correlation length of the porous structure. To quantitively analyze the structural differences among the carbon spheres, the experimental data are fitted using the Debye model, as expressed by the following equation:

$$I(q) = \frac{A}{q^4} + \frac{B' {a_1}^4}{\left(1 + {a_1}^2 q^2\right)^2} + D \quad (1)$$

where A is related to the scattering intensity from the outer surface of the carbon spheres, B' represents the density correlation intensity of the internal structure, a_1 denotes the characteristic length scale, and D corresponds to the background scattering. The radius of gyration R_g, defined as the root mean square distance from the center of mass, is used to characterize the size of the scattering object (*i.e.*, the nanopore), and its relationship with a_1 is given by $R_g = a_1 \times \sqrt{6}$.[33] Fig. 3(g) shows the fitted a_1 values of PNHCs and NPNHCs at different carbonization temperatures, with the detailed fitting curves provided in Fig. S3 and S4. As the carbonization temperature increases, the a_1 values of both sample series exhibit a gradual upward trend, indicating an increase in the characteristic size of nanoporous structures within the carbon matrix. Notably, the a_1 values of NPNHC samples are consistently higher than those of PNHC samples at all temperature points. This suggests that the involvement of NH_3 during the carbonization process promotes the formation of larger pore structures, which may be attributed to enhanced structural disorder, increased defect density, and the removal of oxygen contained functional group.[23,34]

Additionally, a comparative analysis is conducted among three types of carbon spheres carbonized at the same temperature (1200 °C): conventional phenolic resin-derived carbon spheres (CPFHC-T1200), cyano-modified phenolic resin-derived carbon spheres (PNHC-T1200), and NH_3-treated cyano-modified carbon spheres (NPNHC-T1200). The SAXS data are analyzed using the Unified fit model proposed by Beaucage,[35] employing the Irena SAS macro for IgorPro to fit the raw data. The total scattering intensity across multiple structural levels is described by the following equation:

$$I(q) \approx \sum_{i=1}^{n} \left(G_i \exp\left(-\frac{q^2 {R_{g_i}}^2}{3} \right) + B_i \exp\left(-\frac{q^2 {R_{g_{(i+1)}}}^2}{3} \right) \times \left\{ \frac{\left[\mathrm{erf}\left(q R_{g_i}/\sqrt{6}\right)\right]^3}{q} \right\} \right) \quad (2)$$

where $I(q)$ is the scattering intensity of all structural levels i. G_i and B_i are the Guinier and Porod prefactors, R_{g_i} is the radius of gyration and P_i is the power-law slope of the corresponding structural level i. For the hard carbon system, two main levels of structure are involved: scattering from the bulk microparticles and from the closed pores. Thus, the structural level is set as 2, where R_{g_2} represents the size of the closed pores and P_2 represents the Porod exponent of the closed pore surface.[36] Fitting results (Fig. 3(h)) reveal that PNHC-T1200, due to the high crosslinking effect induced by cyano modification, forms a denser structure with smoother pore walls upon carbonization, resulting in a larger absolute value of P, which is 3.69. In contrast, both CPFHC-T1200 and NPNHC-T1200 exhibit similar P values of 2.93 and 2.7 (Fig. 3(i)), respectively, indicating a comparable degree of pore wall roughness. Notably, NPNHC-

T1200 maintains a low specific surface area while still exhibiting pore wall roughness comparable to that of CPFHC-T1200. This indicates that NH_3 treatment not only alters the evolution of carbon layer structures but also significantly increases the pore wall roughness, thereby introducing more accessible and effective sodium storage sites.[23,37] Moreover, the characteristic size values (R_g) obtained from the Unified model fitting are in strong agreement with those obtained independently through Debye model fitting, verifying the reliability and consistency of the Unified approach. The fitted pore sizes and structural features are further corroborated by high-resolution transmission electron microscopy (HR-TEM) observations.

Fig. 4 presents the microstructural features of three carbon spheres-CPFHC-T1200 (derived from unmodified phenolic resin), PNHC-T1200, and NPNHC-T1200-and establishes the structural correlation among their BET results, HRTEM images, and schematic illustrations of pore morphology. CPFHC-T1200 (39.66 m^2 g^{-1}, as shown in Fig. S5) displays a large number of pores with rough walls, as evidenced by both TEM and schematic representations. PNHC-T1200 (4.24 m^2 g^{-1}), prepared from cyano-modified resin without NH_3 treatment, shows smoother and fewer pores, indicating the formation of a compact closed-pore structure due to high crosslinking density. In contrast, NPNHC-T1200 (1.87 m^2 g^{-1}), which underwent NH_3-assisted carbonization, maintains a low surface area, but its pore walls become significantly rougher and more disordered. These visual differences are in good agreement with SAXS-based surface roughness analysis: PNHC-T1200 exhibits the smoothest internal pore surfaces, while NPNHC-T1200 shows roughness comparable to CPFHC-T1200. NH_3 treatment disrupts the originally compact carbon layer arrangement during pyrolysis, generating rougher and more defect-rich pore walls. This structural transformation, despite the preservation of a low overall surface area, leads to the formation of more accessible internal structures and provides additional sodium storage sites.[34,38,39]

Fig. 5(a) and (b) show the galvanostatic charge/discharge profiles of the PNHC and NPNHC anodes at a current density of 30 mA g^{-1} (0.1C). According to the initial charge–discharge curves, the total reversible capacity can be clearly divided into two regions: a sloping region above 0.1 V and a plateau region below 0.1 V. As the carbonization temperature increases from 1000 °C to 1600 °C, the initial discharge capacities of the NPNHC electrodes are 364.40, 364.45, 358.02, and 349.98 mAh g^{-1}, with corresponding initial ICEs of 78.73%, 81.81%, 88.28%, and 88.08%, respectively. The ICEs of the corresponding PNHC electrodes are 68.4%, 78.11%, 88.27%, and 87.08%. Compared to the PNHC samples carbonized at the same temperature (Fig. 5(c)), the ICEs of NPNHC-T1000 and NPNHC-T1200 are improved by 10.33% and 3.7%, respectively. This indicates that introducing NH_3 prior to 500 °C effectively regulates the structural evolution of the carbon matrix during the intermediate pyrolysis stage, thereby enhancing the initial efficiency.[33,37] It is worth noting that while most hard carbon materials with high ICE typically require higher carbonization temperatures (above 1400 °C) to achieve low surface area and closed-pore structures, our NPNHC-T1200 sample delivers an exceptionally low surface area of 1.87 m^2 g^{-1} and a high ICE of 81.81% at only 1200 °C, demonstrating great potential for achieving high performance under milder carbonization conditions (as summarized in Table 1). Combined with the previously discussed BET and SAXS results, the NPNHC-T1200 sample maintains a relatively

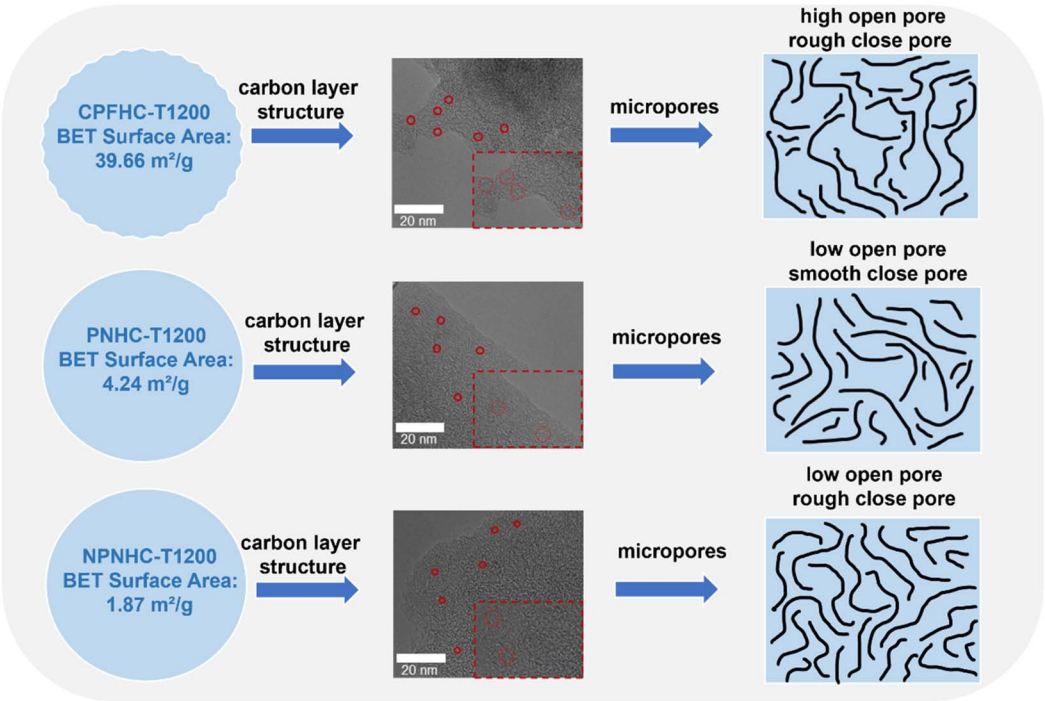

Fig. 4 Comparison of BET surface area, HRTEM images, and pore structure schematics of CPFHC, PNHC, and NPNHC carbonized at 1200 °C.

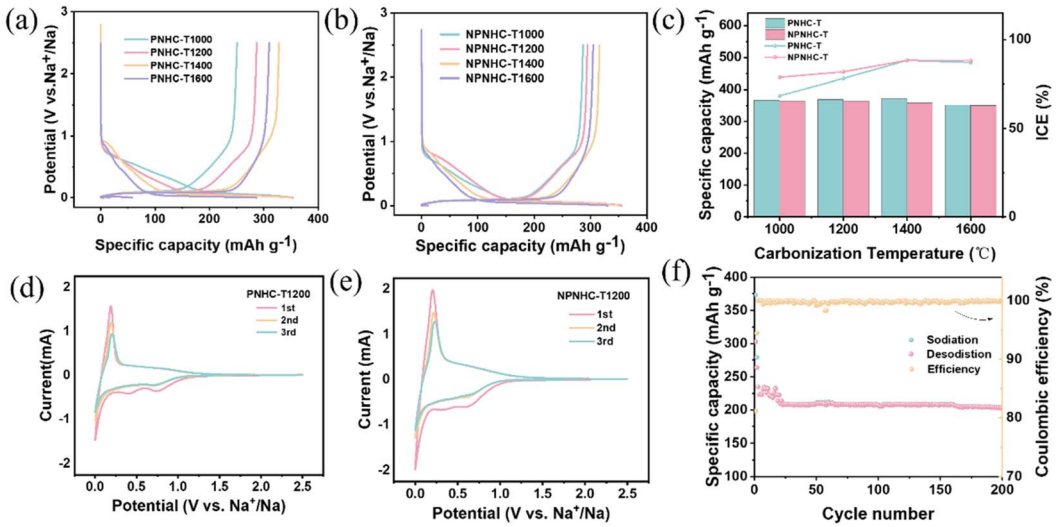

Fig. 5 Electrochemical performance of the carbon sphere anodes. (a) First-cycle galvanostatic charge/discharge curve of PNHC samples at 0.1C; (b) first-cycle galvanostatic charge/discharge curve of NPNHC samples at 0.1C; (c) comparison of ICE and first-cycle discharge capacity between the two types of carbon sphere anodes; (d) CV curves of PNHC-T1200; (e) CV curves of NPNHC-T1200; (f) cycling performance of NPNHC-T1200 at 0.1C.

low specific surface area while its closed-pore structure undergoes a transition from smooth to rough. This structural evolution effectively suppresses excessive formation of the solid electrolyte interphase (SEI), thereby reducing irreversible sodium loss during the first cycle. Meanwhile, the moderately rough pore walls provide more accessible and efficient sodium storage sites, consequently leading to a synergistic enhancement in ICE.

Cyclic voltammetry (CV) measurements are performed on PNHC and NPNHC electrodes, as shown in Fig. 5(d), (e), S6 and S7. In the first cycle, all samples exhibit a pronounced irreversible cathodic peak, which can be attributed to the formation of the SEI and partial irreversible sodium insertion. The intensity of the redox peaks and the degree of overlap between successive cycles vary significantly with carbonization temperature. Among the tested samples, NPNHC-T1200 displays the most favorable electrochemical behavior, featuring the strongest cathodic peak and excellent overlap in subsequent cycles-indicative of enhanced Na^+ diffusion kinetics and cycling stability.[50] Overall, NPNHC-T1200 achieves an optimal trade-off between electrochemical activity and reversibility. A comparison with PNHC-T1200 further confirms that NH_3 treatment significantly improves redox kinetics and cycle stability, underscoring the structural advantages of this strategy. NPNHC-T1200 possesses moderately rough pore walls, which provide a more favorable microenvironment for reversible sodium storage. This structural optimization is also reflected in the CV profiles. The sloping region is mainly associated with Na^+ adsorption at defect sites and interlayer insertion, while the plateau region can be attributed to Na^+

Table 1 Comparison of the specific surface area and initial coulombic efficiency (ICE) of NPNHC-T1200 with previously reported carbon-based materials

Sample	Cabonization temperature (°C)	Surface area (m^2 g^{-1})	ICE (%)	Reference
Thermosetting phenolic resin	1250	219.5	60.2	7
Sucrose and phenolic resin	1400	1.54	87	40
Microporous phenolic resin	1300	539	81	41
Microporous phenolic resin	1500	84.6	85	41
Phenolic resin	1300	2.42	80.69	42
Sawdust	1200	6.7	75.5	43
Corncob	1200	7.64	63.6	44
Bagasse	1200	49	68	45
Lignin	1600	4	81.2	46
Peanut shell	1400	239	55.6	47
Vine shoots	1200	3.13	71.2	48
Corncob	1400	6.05	66.59	49
NPNHC	1200	1.87	81.81	This work

adsorption on the internal surfaces of closed pores. The moderately rough closed-pore walls in NPNHC-T1200 not only suppress excessive SEI formation but also facilitate efficient ion transport, thereby regulating the relative contributions of these processes. As a result, the CV curves exhibit well-defined and stable features that are in good agreement with the high ICE and cycling stability of the optimized samples.[51]

As shown in Fig. 5(f), the NPNHC-T1200 sample exhibits the most superior long-term cycling stability among all samples at a current density of 0.1C. After 200 cycles, it maintains a reversible capacity of 203.5 mAh g^{-1} and a capacity retention of 97.2% (computed between the last cycles and the first ones after the first 20, necessary for stabilization), which is significantly superior to the samples prepared at other temperatures.[52] NPNHC-T1200 achieves an optimal balance between ICE (81.81%) and long-term cycling capacity. This superior performance can be attributed to its structural characteristics: the material maintains a relatively low specific surface area while exhibiting abundant close pores with rough pore-wall morphology. In addition, the effective retention of nitrogen in NPNHC-T1200 enhances the contents of pyrrolic N, pyridinic N, and graphitic N, providing abundant active sites for reversible sodium storage, suppressing irreversible reactions, and thus contributing to the synergistic improvement of capacity retention and structural stability.[53,54]

To further investigate the electrochemical behavior of the carbon spheres in sodium-ion batteries, EIS measurements are conducted on both the PNHC and NPNHC series. The corresponding Nyquist plots are shown in Fig. 6(a) and (b). All samples exhibit typical impedance characteristics, consisting of a high-frequency semicircle and a low-frequency inclined line. The spectra are fitted using an equivalent circuit model comprising R_Ω (bulk resistance), R_{ct} (charge transfer resistance), C_d (double-layer capacitance), and Z_w (Warburg diffusion impedance). Among these, R_{ct} primarily reflects the ease of charge transfer at the electrode–electrolyte interface, a process closely related to sodium-ion intercalation into graphite-like interlayers or closed nanopores in hard carbon materials.[6] Overall, across various carbonization temperatures, the NPNHC series exhibit slightly lower R_{ct} values than the PNHC series, with NPNHC-T1200 showing the lowest charge transfer resistance, indicating the most favorable interfacial reaction kinetics. Although the impedance differences between the two series are not significant, their distinct cycling performances suggest that the introduction of NH_3 in the early carbonization stage may promote the regulation of pore-wall roughness and structural defects. Moderately rough pore walls are conducive to the formation of a more uniform and stable SEI layer and offer additional interfacial active sites, thereby reducing interfacial resistance and facilitating coupled electron/ion transport.[37]

To investigate the sodium-ion diffusion behavior of the hard carbon materials, GITT tests are conducted. The sodium-ion diffusion coefficient (D_{Na^+}) is determined during the second charge–discharge cycle using the GITT method based on Fick's second law. The calculation formula is as follows:

$$D_{Na^+} = \frac{4}{\pi\tau}\left(\frac{m_B V_m}{M_B S}\right)^2 \left(\frac{\Delta E_s}{\Delta E_\tau}\right)^2 \quad (3)$$

Here, τ (s) represents the duration of a single current pulse, m_B (g) is the actual mass of the active material (hard carbon) in the working electrode, V_m (mL mol^{-1}) denotes the molar volume, M_B (g mol^{-1}) is the molar mass, S (cm^2) is the active surface area of the working electrode, while ΔE_s (V) and ΔE_τ (V) refer to the potential difference between two adjacent steady states and the voltage change induced by the current pulse, respectively.[6]

As shown in Fig. 6(c)–(f), it can be observed that the D_{Na^+} during the sodiation process can be divided into three stages: in the initial stage, when the potential is above 0.1 V, the D_{Na^+}

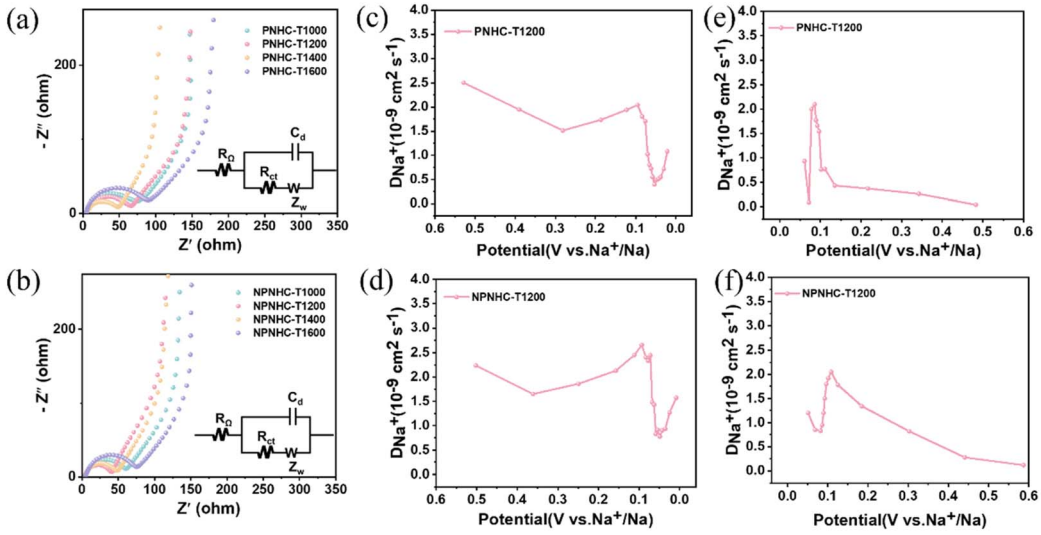

Fig. 6 Electrochemical kinetics analysis of the carbon sphere anodes. (a) EIS spectrum and corresponding equivalent circuit of PNHC; (b) EIS spectrum and corresponding equivalent circuit of NPNHC; (c and d) variation of the sodium-ion diffusion coefficient at different potentials during the second charge/discharge cycle of PNHC-T1200; (e and f) variation of the sodium-ion diffusion coefficient at different potentials during the second charge/discharge cycle of NPNHC-T1200.

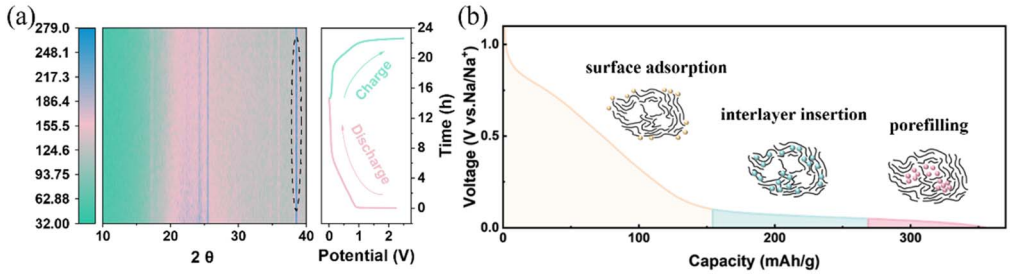

Fig. 7 (a) *In situ* XRD patterns of the carbon electrode recorded during the first charge–discharge cycle, showing the evolution of diffraction peaks with time and potential, which reflects the structural response of hard carbon to sodium (de)intercalation. The right panel presents the corresponding charge–discharge profiles to illustrate the potential regions of phase changes, (b) schematic illustration of the sodium storage mechanism in hard carbon, where the sloping region is attributed to Na^+ adsorption on defects and pore surfaces, the transition region corresponds to Na^+ filling in closed pores, and the plateau region originates from Na^+ intercalation between graphene-like layers.

gradually decreases with decreasing potential, corresponding to the rapid surface adsorption of sodium ions on the hard carbon. At this stage, the diffusion paths are short and the kinetics are relatively fast. In the second stage, as the potential approaches 0.1 V, D_{Na^+} drops sharply and reaches a minimum value around 0.05 V, which is attributed to the interlayer insertion of sodium ions. The narrow interlayer spacing and limited diffusion channels result in significantly restricted diffusion behavior. In the third stage, when the potential drops below 0.05 V, D_{Na^+} increases again, indicating the gradual filling of closed pores or defect-rich regions by sodium ions. These structures may offer additional accessible active sites and alternative diffusion pathways. The three-stage behavior is consistent with the synergistic sodium storage mechanism involving surface adsorption, interlayer insertion, and pore filling, further confirming the coexistence of multiple sodium storage pathways in hard carbon and their correlation with the structure–performance relationship.[13,25]

Further comparison of the sodium-ion diffusion behavior across the three sodiation stages reveals that the D_{Na^+} values of NPNHC-T1200 are significantly higher than those of PNHC-1200 over the entire voltage range. In the low-potential region (<0.05 V), where sodium ions begin to fill closed pores, NPNHC-T1200 exhibits a more pronounced increase in D_{Na^+}. Previous studies have shown that increased pore wall roughness is closely associated with enhanced diffusion channel complexity, which effectively facilitates continuous ion transport and improves storage kinetics. Based on its structural characteristics, NPNHC-T1200 possesses a higher degree of pore wall roughness, which introduces more defect sites and tortuous diffusion pathways within the closed-pore regions. These features expand the accessible space for sodium-ion migration. The increased complexity of diffusion paths contributes to reduced ion migration resistance and improved pore-filling diffusion behavior, thereby enabling a more efficient sodium storage process.[33,37]

The *in situ* XRD results (as shown in Fig. 7(a)) clearly reveal the structural evolution of the hard carbon material during the first charge–discharge cycle under a constant current of 0.1C. By correlating the voltage–capacity curve with the XRD patterns (as shown in Fig. 7(b)), the sodium insertion process can be divided into three stages: adsorption, intercalation, and pore filling.[25,55] At the initial stage of sodiation (>0.2 V), the capacity increases rapidly, yet no obvious changes are observed in the diffraction peaks, indicating that sodium ions are primarily stored through physical adsorption onto surface defects, edges, or functional groups of the hard carbon, without inducing notable structural evolution. As the potential further decreases to the range of approximately 0.1–0.2 V, a slight shift or broadening of the main diffraction peak (~22°) is observed, indicating a reversible expansion and contraction of the interlayer spacing. This behavior is attributed to the intercalation of sodium ions into the interlayer galleries of nanocrystalline graphite domains. Although the overall structure is disordered, a limited number of ordered graphene-like regions remain, allowing partial intercalation. When the potential drops below 0.1 V, the capacity continues to increase while the XRD peaks and intensity remain unchanged, suggesting that sodium ions are primarily filling microporous structures in this stage. These storage sites lack long-range order and thus are difficult to detect by XRD.[50,56,57] Based on the results of *in situ* XRD and GITT, the hard carbon material exhibits a typical synergistic sodium storage mechanism involving adsorption, intercalation, and pore filling.

4 Conclusion

In summary, we have developed an NH_3-assisted carbon structure engineering strategy to regulate closed-pore structures in cyano-functionalized phenolic resin-derived hard carbons. This approach enables controllable roughness of closed pores while maintaining ultra-low surface area, thereby balancing ICE, capacity, and cycling stability. The optimized materials demonstrate enhanced sodium-ion diffusion kinetics and improved long-term reversibility. More importantly, this work reveals the critical role of closed-pore surface characteristics in sodium storage and offers a feasible guideline for designing advanced carbon anodes in sodium-ion batteries.

Conflicts of interest

There are no conflicts of interest to declare.

Data availability

The data generated or analyzed in this study are available upon reasonable request from the corresponding author.

Supplementary information: additional experimental details and characterization data, which further illustrate and validate the conclusions presented in the main text. See DOI: **https://doi.org/10.1039/d5ra05188f**.

Acknowledgements

This work is financially supported by the National Key Research and Development Program of China (Grant No. 2021YFA0715801) and Natural Science Foundation of Beijing Municipal (No. 2254105).

References

1 Q. Wei, Y. Fu, G. Zhang, Y. Wang, X. Wang, M. Mohamedi and S. Sun, *RSC Adv.*, 2016, **6**, 84149–84154.
2 L. Kitsu Iglesias, S. D. Marks, N. Rampal, E. N. Antonio, R. de Ferreira de Menezes, L. Zhang, D. Olds, S. E. Weitzner, K. G. Sprenger, L. F. Wan and M. F. Toney, *Small*, 2025, **17**, 2505561.
3 Y.-N. Cui, T.-J. Jiang, Q.-q. Guan, L. Liu, G. Yang, P.-F. Wang, Y.-H. Zhang, L.-Y. Tian, Y.-H. Li and F.-N. Shi, *J. Alloys Compd.*, 2025, **1027**, 180641.
4 J. Yu, X. Sun, X. Shen, D. Zhang, Z. Xie, N. Guo and Y. Wang, *Energy Storage Mater.*, 2025, **76**, 104134.
5 W. Xia, S. Zheng, L. Qiu, H. Hu, Y. Chen, S. Wei and H. Zhou, *Pol. J. Environ. Stud.*, 2025, DOI: **10.15244/pjoes/203046**.
6 C. Fan, R. Zhang, X. Luo, Z. Hu, W. Zhou, W. Zhang, J. Liu and J. Liu, *Carbon*, 2023, **205**, 353–364.
7 H.-l. Wang, Z.-q. Shi, J. Jin, C.-b. Chong and C.-y. Wang, *J. Electroanal. Chem.*, 2015, **755**, 87–91.
8 Q. Wang, X. Zhu, Y. Liu, Y. Fang, X. Zhou and J. Bao, *Carbon*, 2018, **127**, 658–666.
9 Y. Li, Z. Wang, L. Li, S. Peng, L. Zhang, M. Srinivasan and S. Ramakrishna, *Carbon*, 2016, **99**, 556–563.
10 Q. Meng, Y. Lu, F. Ding, Q. Zhang, L. Chen and Y.-S. Hu, *ACS Energy Lett.*, 2019, **4**, 2608–2612.
11 D. Li, H. Chen, G. Liu, M. Wei, L.-x. Ding, S. Wang and H. Wang, *Carbon*, 2015, **94**, 888–894.
12 S. Xiao, Y. J. Guo, H. X. Chen, H. Liu, Z. Q. Lei, L. B. Huang, R. X. Jin, X. C. Su, Q. Zhang and Y. G. Guo, *Adv. Mater.*, 2025, **37**, 202501434.
13 Y. Sun, T. Shen, H. Pan, Z. He, B. Ru, G. Dai and S. Wang, *Appl. Surf. Sci.*, 2025, **680**, 161422.
14 Q. Hu, L. Xu, G. Liu, J. Hu, X. Ji and Y. Wu, *ACS Nano*, 2024, **18**, 21491–21503.
15 L. Yang, M. Hu, H. Zhang, W. Yang and R. Lv, *J. Colloid Interface Sci.*, 2020, **566**, 257–264.
16 S. Tao, W. Xu, J. Zheng, F. Kong, P. Cui, D. Wu, B. Qian, S. Chen and L. Song, *Carbon*, 2021, **178**, 233–242.
17 Z.-T. Liu, T.-H. Hsieh, C.-W. Huang, C. Kwon, J. Li, J.-Y. You, C.-J. Lin and W.-R. Liu, *Electrochim. Acta*, 2025, **534**, 146552.
18 X. Zhong, Y. Li, L. Zhang, J. Tang, X. Li, C. Liu, M. Shao, Z. Lu, H. Pan and B. Xu, *ACS Appl. Mater. Interfaces*, 2019, **11**, 2970–2977.
19 X. Y. Bu, Y. L. Zhu, C. J. Wang, W. Li, Y. Xia and Y. Zhao, *ACS Appl. Mater. Interfaces*, 2024, **16**, 7200–7210.
20 P. Varasteanu, C. Romanitan, A. Bujor, O. Tutunaru, G. Craciun, I. Mihalache, A. Radoi and M. Kusko, *Nanomaterials*, 2020, **10**, 2321.
21 B. Tratnik, N. Van de Velde, I. Jerman, G. Kapun, E. Tchernychova, M. Tomšič, A. Jamnik, B. Genorio, A. Vizintin and R. Dominko, *ACS Appl. Energy Mater.*, 2022, **5**, 10667–10679.
22 Y. Liu, S. Dai, J. Deng, D. Jiang, X. Ji, Q. Meng, H. Wang and L. Liu, *J. Colloid Interface Sci.*, 2025, **686**, 136–150.
23 T. Liu, T. Kou, D. Bulmahn, C. Ortuno-Quintana, G. Liu, J. Q. Lu and Y. Li, *ACS Appl. Energy Mater.*, 2018, **1**, 5043–5053.
24 E. Olsson, J. Cottom and Q. Cai, *Small*, 2021, **17**, e2007652.
25 Y. Huang, Y. Wang, P. Bai and Y. Xu, *ACS Appl. Mater. Interfaces*, 2021, **13**, 38441–38449.
26 C. Chen, Y. Huang, Y. Zhu, Z. Zhang, Z. Guang, Z. Meng and P. Liu, *ACS Sustainable Chem. Eng.*, 2020, **8**, 1497–1506.
27 C. Chen, Y. Lu, Y. Ge, J. Zhu, H. Jiang, Y. Li, Y. Hu and X. Zhang, *Energy Technol.*, 2016, **4**, 1440–1449.
28 J. Hou, X. Mao, J. Wang, C. Liang and J. Liang, *Chem. Phys.*, 2021, **551**, 111352.
29 I. Alouiz, M. Aqil, A. Chari, M. Dahbi, M. Y. Amarouch and D. Mazouzi, *RSC Adv.*, 2025, **15**, 19546–19560.
30 S. Jha, Y. Qin, Y. Chen, Z. Song, L. Miao, Y. Lv, L. Gan and M. Liu, *J. Mater. Chem. A*, 2025, **13**, 15101–15110.
31 A. Beda, F. Rabuel, M. Morcrette, S. Knopf, P.-L. Taberna, P. Simon and C. Matei Ghimbeu, *J. Mater. Chem. A*, 2021, **9**, 1743–1758.
32 L. Guo, C. Qiu, R. Yuan, X. Li, X. Li, K. Li, W. Zhu, X. Liu, A. Li, H. Liu, X. Chen and H. Song, *ACS Appl. Mater. Interfaces*, 2024, **16**, 27419–27428.
33 D. A. Stevens and J. R. Dahn, *J. Electrochem. Soc.*, 2000, **147**, 4428–4431.
34 S. Li and Z. Fan, *Microporous Mesoporous Mater.*, 2019, **274**, 313–317.
35 G. Beaucage, T. A. Ulibarri, E. P. Black and D. W. Schaefer, Multiple Size Scale Structures in Silica—Siloxane Composites Studied by Small-Angle Scattering, *Hybrid Organic-Inorganic Composites*, Sandia National Laboratories, Albuquerque, 1995.
36 D. Tang, Y. Zhao, D. Han, Y. Pan and Y. Xie, *Constr. Build. Mater.*, 2023, **409**, 134002.
37 D. Saurel, J. Segalini, M. Jauregui, A. Pendashteh, B. Daffos, P. Simon and M. Casas-Cabanas, *Energy Storage Mater.*, 2019, **21**, 162–173.
38 Y. Zhang, X. Li, P. Dong, G. Wu, J. Xiao, X. Zeng, Y. Zhang and X. Sun, *ACS Appl. Mater. Interfaces*, 2018, **10**, 42796–42803.
39 H. Tonnoir, D. Huo, R. L. S. Canevesi, V. Fierro, A. Celzard and R. Janot, *Mater. Today Chem.*, 2022, **23**, 2468–5194.
40 H. Zhang, H. Ming, W. Zhang, G. Cao and Y. Yang, *ACS Appl. Mater. Interfaces*, 2017, **9**, 23766–23774.

41 A. Kamiyama, K. Kubota, T. Nakano, S. Fujimura, S. Shiraishi, H. Tsukada and S. Komaba, *ACS Appl. Energy Mater.*, 2019, **3**, 135–140.
42 Z. Wei, H.-X. Zhao, Y.-B. Niu, S.-Y. Zhang, Y.-B. Wu, H.-J. Yan, S. Xin, Y.-X. Yin and Y.-G. Guo, *Mater. Chem. Front.*, 2021, **5**, 3911–3917.
43 J. Wang, F. Li, Y. Duan, H. Tao and X. Yang, *Ionics*, 2023, **29**, 2311–2318.
44 P. Liu, Y. Li, Y.-S. Hu, H. Li, L. Chen and X. Huang, *J. Mater. Chem. A*, 2016, **4**, 13046–13052.
45 K. Yu, X. Wang, H. Yang, Y. Bai and C. Wu, *J. Energy Chem.*, 2021, **55**, 499–508.
46 M. Chen, F. Luo, Y. Liao, C. Liu, D. Xu, Z. Wang, Q. Liu, D. Wang, Y. Ye, S. Li, D. Wang and Z. Zheng, *J. Electroanal. Chem.*, 2022, **919**, 116526.
47 H. Yu, Y. Meng, D. Qi, Q. Xiang and F. Zhu, *J. Power Sources*, 2025, **658**, 238353.
48 D. Alvira, D. Antorán, M. Vidal, V. Sebastian and J. J. Manyà, *Batteries Supercaps*, 2023, **6**, e202300233.
49 N. J. Song, N. Guo, C. Ma, Y. Zhao, W. Li and B. Li, *Molecules*, 2023, **28**, 3595.
50 Z. Tang, R. Zhang, H. Wang, Y. Huang, D. Sun, S. Zhou, Z. Pan, Y. Tang, X. Ji, K. A. Amine and M. Shao, *Nat. Commun.*, 2023, **14**, 6024.
51 P. Liu, Z. Song, Q. Huang, L. Miao, Y. Lv, L. Gan and M. Liu, *Energy Environ. Sci.*, 2025, **18**, 5397–5406.
52 N. Pianta, D. A. Florenzano, R. Lorenzi, L. Navarini, C. Santoro and R. Ruffo, *Adv. Sustainable Syst.*, 2025, **9**, 2500027.
53 Y. Qu, M. Guo, X. Wang and C. Yuan, *J. Alloys Compd.*, 2019, **791**, 874–882.
54 D. Zhang, X. Zhang, F. Li, K. Cai, Z. Zheng and L. Li, *J. Electrochem. Soc.*, 2025, **172**, 050522.
55 T. Feng, L. He, F. Song, Y. Li and Q. Chen, *Carbon*, 2025, **241**, 120389.
56 P. Zhang, Y. Shu, Y. Wang, J. Ye and L. Yang, *J. Mater. Chem. A*, 2023, **11**, 2920–2932.
57 Y. Gao, *Earth Environ. Sci.*, 2021, **804**, 032025.